Geophysical Research Letters

RESEARCH LETTER
10.1029/2022GL099487

Transcrustal Compressible Fluid Flow Explains the Altiplano-Puna Gravity and Deformation Anomalies

J. Gottsmann[1], E. Eiden[2], and M. E. Pritchard[2]

[1]School of Earth Sciences, University of Bristol, Bristol, UK, [2]Department of Earth and Atmospheric Sciences, Cornell University, Cornell, NY, USA

Key Points:

- We report gravity changes between 2010 and 2018 from the Altiplano-Puna deformation anomaly
- Numerical modeling highlights minor density changes in the subsurface magmatic plumbing system
- 2010–2018 deformation best explained by transcrustal migration of compressible magmatic fluids

Supporting Information:

Supporting Information may be found in the online version of this article.

Correspondence to:

J. Gottsmann,
gljhg@bristol.ac.uk

Citation:

Gottsmann, J., Eiden, E., & Pritchard, M. E. (2022). Transcrustal compressible fluid flow explains the Altiplano-Puna gravity and deformation anomalies. *Geophysical Research Letters*, *49*, e2022GL099487. https://doi.org/10.1029/2022GL099487

Received 11 MAY 2022
Accepted 5 AUG 2022

Author Contributions:

Conceptualization: J. Gottsmann, M. E. Pritchard
Formal analysis: J. Gottsmann, E. Eiden
Funding acquisition: J. Gottsmann, M. E. Pritchard
Investigation: J. Gottsmann, E. Eiden
Methodology: J. Gottsmann
Project Administration: J. Gottsmann, M. E. Pritchard
Software: J. Gottsmann
Supervision: M. E. Pritchard
Validation: J. Gottsmann
Visualization: J. Gottsmann
Writing – original draft: J. Gottsmann
Writing – review & editing: J. Gottsmann, E. Eiden, M. E. Pritchard

Abstract Enigmatic large-scale (>150 km wide) ground deformation in southern Bolivia has been ongoing for more than 50 year. Concurrent changes in gravity recorded between 2010 and 2018 imply minor changes in subsurface density in the absence of significant mass changes. Numerical modeling of the gravity changes and concurrent InSAR LOS displacements gives annual bulk density changes of 0.002 kg m^{-3} in the Altiplano-Puna Magma Body (APMB) and −0.03 kg m^{-3} in a vertical bulge-column ensemble beneath Uturuncu volcano. We propose that the transcrustal migration of fluids from the APMB to shallower crustal levels by compressible flow is the source of ground deformation. Localized ground subsidence south of Uturuncu can be best explained by a density decrease of 20 ± 5 kg m^{-3} between 2011 and 2013 in a hydrothermal reservoir. Our findings contribute to the growing recognition of transcrustal fluid migration as a source of volcanic unrest.

Plain Language Summary Large-scale (>80 km wide) anomalous ground uplift has been observed in the Altiplano-Puna region of southern Bolivia for more than five decades, but there is no consensus on the underlying causes. While magma migration and emplacement at shallow depth or a combination of magma and fluid migration have been proposed, none of the previous studies considered changes in the gravity field. Here, we report on temporal and spatial changes in gravity observed between 2010 and 2018 which primarily indicate subsurface density changes as the cause of ground deformation during that period. Using computer modeing, we show that the ascent of fluids from a deep-seated (~20 km below the ground surface) magma reservoir through the overlying crust can explain both the deformation and gravity changes. This ascent occurs amid a decrease in confining pressure, leading to the expansion of the fluids within a volume best characterized by a column-like geometry. Movement of magma is either negligible or absent. Localized ground subsidence can be explained by the release of the fluids to the surface.

1. Introduction

Periods of unrest characterized by an unusual behavior of a volcano which is cause for concern are ubiquitous manifestations of sub-surface processes underpinning active volcanism (Biggs et al., 2014; Phillipson et al., 2013). At volcanoes with seemingly protracted (hundreds of kyears) absence of eruptive activity such as at Uturuncu volcano (22.270°S, 67.180°W) in the Altiplano-Puna region of southern Bolivia, the recognition of unrest is therefore startling (Sparks et al., 2008). The 6,008 m high Pleistocene dacitic volcano forms part of the Altiplano-Puna volcanic complex (APVC; de Silva, 1989) and sits in the center of a large (~150 km in diameter) and temporally protracted deformation anomaly, recognized by satellite remote sensing and geodetic leveling (Gottsmann et al., 2017; Pritchard & Simons, 2004). Mean deformation velocities reached values of ~1 cm yr^{-1} in the line-of-sight (LOS) of satellite radar between 1992 and 2011, with mean maximum orthometric uplift of 1.2 ± 0.2 cm yr^{-1} between 1965 and 2011. A moat of ground subsidence surrounds the area of ground uplift, where maximum subsidence rates reached 0.3 ± 0.03 cm yr^{-1} between 1965 and 2011 (Gottsmann et al., 2018; S. T. Henderson & Pritchard, 2013). GNSS observations at station UTUR between 2010 and 2020 indicate a slowing of ground uplift to maximum values of 0.32 ± 0.05 cm yr^{-1} (Eiden et al., 2021). The region is host to the Altiplano-Puna Magma Body (APMB), a ~10 km thick zone of low seismic velocities and high electrical conductivity with its surface at 10–15 km below sea level (Comeau et al., 2016; Ward et al., 2014; Zandt et al., 2003).

Several models have been proposed to explain the source of ground deformation including elastic half-space models of material exchange between deep-seated sources and shallow-seated sinks (S. T. Henderson & Pritchard, 2013), models of diapiric ascent of magma from the APMB (Fialko & Pearse, 2012), thermomechanical models of single source pressurization (Hickey et al., 2013) and material transfer between the APMB and a

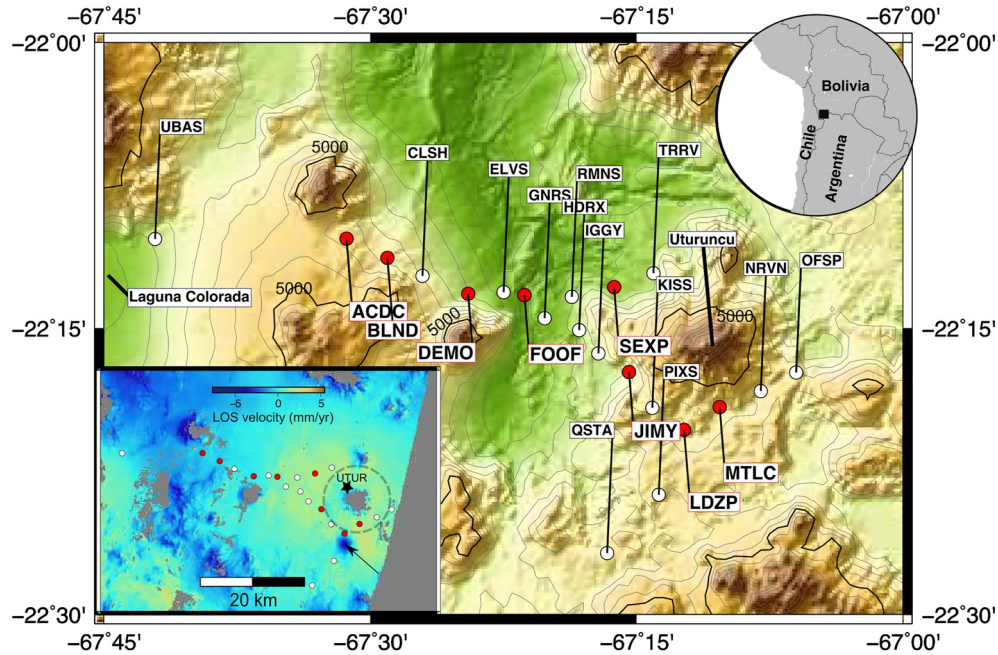

Figure 1. Survey area, benchmark locations (white and red circles), and identifiers. Benchmarks with longest temporal coverage (4–6 occupations between 2010 and 2018) are marked by red circles. Lower left inset: InSAR LOS displacements (mm/yr) from Sentinel-1 track 156 (11.2014–11.2018) with respect to reference station UBAS. Locations of Uturuncu's summit, cGNSS station UTUR (black star in inset) and Laguna Colorada are shown for reference. The black arrow in the inset marks an area of localized ground subsidence south of Uturuncu (Lau et al., 2018) and the broken line indicates the footprint of the modeled column shown in Figure 2.

vertically extensive transcrustal low-density body (Gottsmann et al., 2017), and a model of magma sill emplacement at the brittle ductile transition zone (Morand et al., 2021). Neither of these models accounts for changes in the gravitational potential associated with the deformation to quantify concurrent density changes. Here, we build on the axisymmetric thermomechanical Finite-Element model presented in Gottsmann et al. (2017) to test whether material transfer from the APMB toward the surface is consistent with observed spatio-temporal variations in the gravity field.

2. Methods

2.1. Gravity Data and Field Surveys

Dynamic gravity data were collected between March 2010 and November 2018 at a network of 20 benchmarks extending from a reference station near Laguna Colorada to the W of Uturuncu along a ∼50 km long survey line toward the east (Figure 1). The resultant gravity change time series includes between two and six occupations at each benchmark with five surveys conducted during the Bolivian summer in November and March between 2010 and 2013; that is, at the beginning and the end of the typical dry season in the Altiplano. The most recent survey was completed in November 2018. Gravity data collection using a Scintrex CG5 (serial number 572) field gravimeter was performed in tandem with GNSS receivers for benchmark locations. Due to the absence of a regional network of GNSS reference stations at the beginning of the survey period and associated large errors in GNSS data we use InSAR LOS data to determine benchmark velocities throughout the study period. We followed standard gravimetric surveying techniques (Battaglia et al., 2008) establishing control points as part of individual survey loops (<3 hr length) to correct for instrument drift and tares due to the shaking of the instrument in harsh terrain. During each individual survey, benchmarks were visited up to six times with at least five cycles of 45 s long readings at 6 Hz during each visit. Data repeatability was generally between 3 and 15 μGal (1μGal = 10^{-8} m s^{-2}) with the higher end of the range at difficult to reach benchmarks and during a period elevated regional seismic activity in October 2012. All gravity data were reduced for tidal (ocean and solid Earth) effects using TSOFT (Van Camp & Vauterin, 2005) using the GOT99.2 (Ray, 1999) and the Wahr-Dehant (Dehant et al., 1999)

latitude-dependent models, respectively. The effect of ground deformation on gravity change is solved implicitly in the model.

2.2. Satellite Geodesy

Synthetic aperture radar (SAR) satellites including European Remote Sensing (ERS-1/2), Envisat, TerraSAR-X (TSX), and Sentinel-1 A/B have measured relative surface displacements along the radar line of sight at Uturuncu from 1992 to present, with some gaps in data availability between 2010 and 2014 (Eiden et al., 2021; Fialko & Pearse, 2012; S. T. Henderson & Pritchard, 2013; Lau et al., 2018). We have used limited TSX data to fill the gap between 2012 and 2014 but could not resolve the small ground velocities we expect to see due to the available scenes in that data set (Eiden et al., 2021). However, based on the GNSS station UTUR (Figure 1), the rate of deformation between 2010 and 2014, is similar within error with the 2014–2018 rate from InSAR (Eiden et al., 2021), indicating no obvious change in ground displacement rate between 2010 and 2018 (Figure S1 in Supporting Information S1). We have processed available Sentinel-1 A/B data for descending track 156 (D156) covering November 2014–2018. The ascending track covering the same region has more noise due to the larger ionospheric effects during acquisition time (Eiden et al., 2021; Liang et al., 2019) and was hence not used in this study. A network of month-long and year-long interferograms was created for D156 using the InSAR Scientific Computing Environment (ISCE, Rosen et al., 2018) on the cloud computing resource Amazon Web Services (S. Henderson & Setiawan, 2020). We use the 30 m Shuttle Radar Topography Mission (SRTM) digital elevation model (DEM) to construct the interferograms (Farr et al., 2007).

The interferometric phase contains atmospheric delays along with the deformation signal (Bevis et al., 1992). We use ISCE to correct for ionospheric effects and the Generic Atmospheric Correction Online Service for InSAR (GACOS) to mitigate tropospheric effects, although these corrections do not remove all atmospheric delay (Rosen et al., 2018; Yu, Li, & Penna, 2018; Yu, Li, Penna, et al., 2018). To generate a time series of ground surface movement at each pixel in the study region, we use the Generic InSAR Analysis Toolbox (GIAnT) and a modified Small Baseline Subset method (Agram et al., 2013; Berardino et al., 2002). Pixels with a coherence under 0.6 are masked.

2.3. Numerical Simulations: Parameterization and Modeling Strategy

Using Cartesian coordinates we jointly and simultaneously solve the constitutive equations behind ground displacement and gravity changes from subsurface density variations $\Delta\rho(x, y, z)$ caused by the concurrent displacement field $\mathbf{u}$ and changes in the gravitational potential ϕ_g arising from the redistribution of mass at depth using 3D Finite Element Analysis (COMSOL Multiphysics 5.4).

Considering elastic deformation in the form of Hooke's law which relates stress σ and strain ϵ via

$$\sigma = 2\mu\epsilon + \lambda \mathrm{tr}(\epsilon) I \tag{1}$$

$$\epsilon = 0.5\left(\nabla \mathbf{u} + (\nabla \mathbf{u})^T\right) \tag{2}$$

We derive eastward, northward and vertical displacement vectors u, v, and w, respectively, directly from the model. Total displacements are projected into the InSAR LOS. μ and λ are the Lamé parameters, $tr(\epsilon)$ is the trace of the strain tensor and I is the identity matrix.

We impose Dirichlet boundary conditions of zero at infinity in order to mathematically close and solve (Cai & Wang, 2005):

$$\nabla^2 \phi_g = -4\pi \ \ G\Delta\rho(x, y, z) \tag{3}$$

where G is the universal gravitational constant.

The vertical component of gravity that is typically measured in volcano gravimetry is calculated from:

$$\Delta g(x, y, z) = \left(-\frac{\delta \phi_g}{\delta z}\right). \tag{4}$$

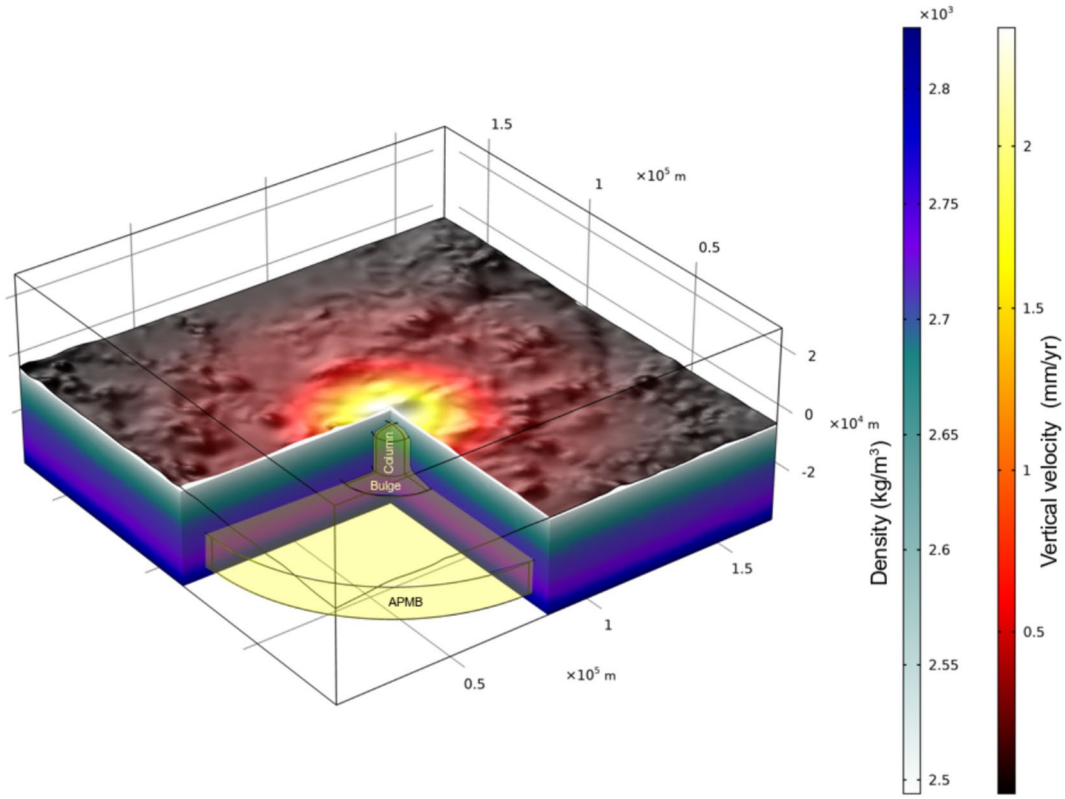

Figure 2. (a) Model dimension and geometry, parameterization of crustal density and predicted best-fit vertical displacements (mm/yr). Boundary conditions of the model domains for the solid mechanics solver are as follows: roller at the sides, fixed at the bottom and free at the ground surface. Source domains are highlighted in transparent yellow and include the APMB- bulge-column (ABC) ensemble.

Residual gravity changes Δg_r account for gravity changes by ground deformation as well as other contributors described in the Supporting Information. The model aims at best-fitting observed gravity residuals and ground displacements by minimizing misfits between observations and model predictions.

The dimensions of the main modeling domain are 160 × 160 × 72 km solving for ~400,000 degrees of freedom (DOF) using ~40,000 mesh elements (ME) for model exploration (Figure 2). Best-fit model mesh refinement increases the number of DOF and ME by a factor of at least 3. We implement a DEM based the SRTM 1 Arc-Second data and set the summit of Uturuncu volcano at $z = 0$ m. The main modeling domain extends from $-36 \text{ km} \leq z \leq 36$ km within which changes in the gravity potential are solved. Stresses and strains in a linearly elastic material are solved for $z < 0$ km, only. Time-depended thermomechanical processes are considered in (Gottsmann et al., 2017) for a protracted (~20 years) time series of InSAR deformation. Such processes are ignored here due to a lack of sufficiently frequent and protracted joint ground deformation and gravity measurements and a significant drop in the rate of ground deformation across the anomaly since 2010 (Eiden et al., 2021). Derived source density and pressure changes as well as resultant subsurface strains affecting changes in gravitational potential should hence be considered upper-bound values.

Following Gottsmann et al. (2017), we parameterize vertical mechanical heterogeneity of the crust by using 3D shear wave velocities (V_s), mineralogical, and density data to derive elastic constants for the model (Brocher, 2005; Lucassen et al., 2001; Ward et al., 2014) (Figure 2; see also Supporting Information for details on data processing). This simplification is acceptable given the very limited lateral variability in V_s values across the region (Ward et al., 2014). The subsurface plumbing system is approximated by a cylindrical domain representing the APMB, with a central bulge extending from its surface to connect to a vertical column. A graphical representation of the model is given in Figure 2 including the dimension and extent of the APMB-bulge-column (ABC) ensemble that reflects the best-fit geodetic model by Gottsmann et al. (2017) based on multiparametric geophysical evidence reported in the Supporting Information.

We first use parameter sweeps of pressure changes in the APMB and the column to obtain a range of optimal least-square fits (minimum misfit and lowest residual) to the InSAR LOS displacements and their uncertainties. This is achieved by rotating the predicted 3D displacement vectors into the line of sight of the satellite observations. The set of statistically plausible vertical displacements determines the free-air contribution to the gravity changes, whereas all displacement vectors contribute to the quantification of gravity changes arising from the shifting of density boundaries in the subsurface. Then density changes in the APMB and the bulge and column are explored using parameter sweeps whereby the density changes in the APMB are initially explored as a fraction of density changes in the bulge and column as to simulate exchange of material between these volumes whilst conserving mass. Finally, a suite of best-fit models for a given combination of observations and their uncertainties is obtained from which optimum values and uncertainty ranges are derived from Monte Carlo sampling for average annual changes given the near-linear trend of gravity and elevation changes over the observation period (Figure 3a).

3. Results and Discussion

Consistent with previous studies, LOS displacements are greatest on the western summit slopes of Uturuncu and decrease to negative values ~40 km from the summit (e.g., Fialko & Pearse, 2012; S. T. Henderson & Pritchard, 2013), although the absolute values of displacement have decreased with time. The mean average LOS velocities derived for the microgravity benchmarks are reported in Table S1 in Supporting Information S1.

Ground displacements and gravity changes are linearly correlated (Figure 3a) and follow a trend which matches within error the theoretical free-air gradient (FAG; -308.6 μGal m^{-1}). The FAG in the survey area is statistically indistinguishable from the theoretical value (del Potro et al., 2013). The correlation between ground displacements and gravity changes along the FAG implies no or only very minor subsurface mass changes amid a decrease in subsurface density (Williams-Jones & Rymer, 2002).

The spatio-temporal evolution of residual gravity changes is shown in Figure 3b for benchmarks with the longest records of observations and in Figure S2 in Supporting Information S1 for the entire network of benchmarks. The overall pattern of residual gravity variations indicates a linear decrease in gravity over a large spatial scale (tens of km) and across the entire survey area. The largest drops in gravity over the 8 yr period are detected at benchmarks closest to Uturuncu's edifice and at two benchmarks located ~45 km to the west of it, with magnitudes reaching -30μGal or a mean average of up to 4μGal yr^{-1}.

Residuals between observations and model predictions for optimal combinations of source parameter changes (Table 1) are shown in Figures 4 and 4b. The best-fit model reproduces mean annual LOS displacements at 18 out of 21 benchmarks within observational errors. The residual of modeled annual ground velocity at LDZP is significantly above data uncertainty, and is explained below. Mean annual residual gravity changes at DEMO, JIMY, LDZP, MTLC, and SEXP are well predicted by the model with residuals between observations and predictions <1 μGal. This implies a steady-state subsurface process behind the observations at Uturuncu. However, residual gravity change residuals at ACDC, BLND, and FOOF are at least two times larger, leading to significant differences between predictions and observations for the duration of the survey (Figure 4).

The derived source parameter changes indicate minor pressure and density variations as the drivers of unrest at Uturuncu. Over the course of the survey, the density of the APMB is predicted to have increased by 0.024 ± 0.016 kg m^{-3} while the density of the bulge and column decreased by 0.176 ± 0.160 kg m^{-3}. Associated volume changes in the APMB are modeled at $-15 \pm 1.6 \times 10^{-6}$ m^3 and $35 \pm 1.6 \times 10^{-6}$ m^3 in the bulge and column. Annual source changes are reported in Table 1.

The simultaneous contraction of the APMB and expansion of the bulge and column explain the sombrero hat deformation pattern observed at Uturuncu, whereby a moat of subsidence surrounds a central area of uplift (e.g., Gottsmann et al., 2017). Our interpretation of the modeling results is that during the observation period material was transferred from the APBM into the column. Given the small source density changes, we propose compressible fluid flow whereby fluids migrate and expand due to a decrease in confining lithostatic pressure from the APMB into the bulge and column as the most likely process behind the unrest between 2010 and 2018. Our model results indicate a statistically significant difference at the 95% probability level in reservoir compressibility

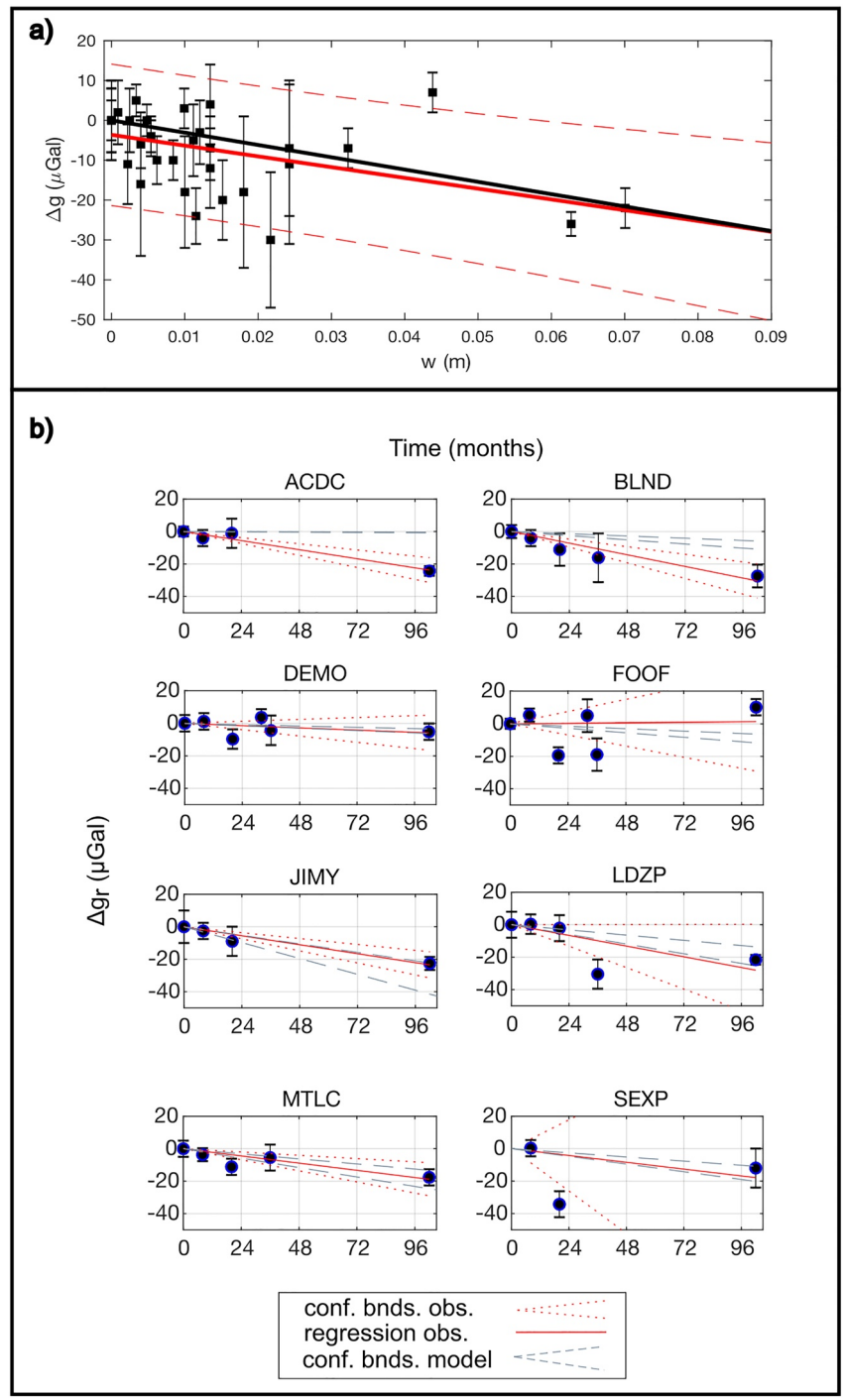

Figure 3. (a) Observed gravity changes Δg as a function of vertical ground displacements w. The red solid line represents the linear fit to observations with 95% confidence intervals marked by red broken lines. The theoretical free-air gradient of -308.6 μGal m^{-1} is shown by the black solid line. The typical uncertainty of displacements (not shown for clarity) is 0.01 m. (b) Residual gravity time series at benchmarks with longest temporal coverage (marked by red circles in Figure 1) including linear regressions through observations with 95% confidence bounds (red) and 95% confidence bounds of model predictions (blue). The time series cover the period March 2010 through November 2018.

Table 1
Best-Fit Annual Changes in Density ($\Delta\rho$), Volume (ΔV) and Pressure (ΔP) of the APMB-Bulge-Column (ABC) Ensemble, Resultant Reservoir Compressibilities, and Respective 1σ Uncertainties

Parameter	Value	1σ
$\Delta\rho_A$	0.002 kg m^{-3}	0.002 kg m^{-3}
$\Delta\rho_{BC}$	−0.03 kg m^{-3}	0.01 kg m^{-3}
ΔV_A	-1.4×10^6 m^3	0.2×10^6 m^3
ΔV_{BC}	3.4×10^6 m^3	0.3×10^6 m^3
ΔP_A	−510 Pa	300 Pa
ΔP_{BC}	5,500 Pa	200 Pa
β_{rA}	1.43 GPa^{-1}	0.25 GPa^{-1}
β_{rBC}	2.22 GPa^{-1}	0.66 GPa^{-1}

(Table 1) between the APMB (1.43 ± 0.25 GPa^{-1}) and the bulge and column (2.22 ± 0.66 GPa^{-1}), consistent with the migration and expansion of fluids throughout a hydraulically connected ABC ensemble.

Magnetotelluric and petrological data allude to an APMB containing ~8 wt% water and evidence for fluid-enhanced seismicity (*b*-values between 1.1 and 1.4 throughout ~75 km of continental crust [Hudson et al., 2022]). The most plausible explanation that satisfies a wide range of available geophysical and petrological constraints on the dynamics and structure beneath the deformation anomaly is therefore a transcrustal migration of fluids from the APMB (and potentially even greater depth) to shallower crustal levels through a permeable vertical columnar structure which feeds the active hydrothermal system of Uturuncu.

It is notable that residual gravity changes are significantly outside model predictions at benchmarks ACDC, BLND, and FOOF, with LDZP undergoing anomalous ground subsidence. These discrepancies allude to local anomalies. The anomaly at LDZP is likely associated with a ~25 km^2 area of ground subsidence to the south of Uturuncu identified between October 2014 and January 2017 in previous studies (Eiden et al., 2021; Lau et al., 2018). We revise our model to include a shallow-seated source of contraction (see Figure S3 in Supporting Information S1) with best-fit pressure and volume changes of −5 MPa yr^{-1}, -0.13×10^6 m^3 yr^{-1} between 2014 and 2018. Best-fit locations are −22.366° and −67.215° with a source center depth of 2.5 ± 0.3 km above sea level. In contrast to the previous modeling of this localized deformation anomaly, our model accounts for stress and strain interactions between different subsurface sources with a prolate geometry for the shallow source providing a better fit to observations than the point sources proposed by (Eiden et al., 2021; Lau et al., 2018). To explain the significant residual gravity change of −22 ± 5 μGal between November 2011 and 2013 a decrease in density of 20 ± 5 kg m^{-3} is required in the shallow source. Our interpretation of the localized ground subsidence is a collapse of a high-level magmatic brine lens extending vertically from the top of the column structure. Numerical modeling by Afanasyev et al. (2018) supports this interpretation whereby lens collapse forms part of the protracted spatio-temporal evolution of high-level brine reservoirs with fluids being supplied to and (after the end of fluid supply) drained from lenses through a high-permeability conduit (i.e., the column in our model). From our gravimetric observations, it appears that the process of lens collapse started sometime between November 2011 and 2013 and hence at least 12 months earlier than identifiable in the InSAR times series giving a duration of the phenomenon of at least 3.5 yr. According to our observations, the anomalous drop in density in the shallow-seated source waned by November 2018 (Figure 2).

At FOOF, anomalous behavior may be associated with water table variations and or/localized stress addand density perturbations along an SW-NE elongated topographic ridge. The ridge is composed of older eroded volcanics at the surface and underlain by >3 km thick material of higher than background density material (labeled anomaly D1 by MacQueen et al., 2021) and shown in Figure 3c for reference). The high-density body is also associated with a positive gravitational tilt angle and interpreted to represent an intrusive complex and/or a zone of disseminated sulfides by MacQueen et al. (2021). Alternatively, the gravity variations may mirror water level perturbations in a river bed which extends NNE-SSW along D1 (FOOF is located at the E shoulder of D1). Although we did not note any drastic changes in river level during the surveys, we cannot rule out gravity perturbations by groundwater level variations or recharge of the hydrothermal system beneath Uturuncu along D1. Benchmarks ACDC and BLND are located along a second SE-NW striking structure composed at the ground surface of an array of deeply eroded sulfide-rich older volcanic edifices ~25 km to the W of D1 and recognizable by local geophysical anomalies: (a) a high positive Bouguer gravity tilt angle (shown in Figure 3c) and (b) a strong electromagnetic conductor labeled C5 in Comeau et al. (2016). In general, tilt angles (the ratio of the first vertical derivative of the potential field to the horizontal gradient) mark subsurface structures with anomalous densities whereby high positive angles are found above anomalously high-density structures (Miller & Singh, 1994) and high negative angles above anomalously low-density structures. Our interpretation of the ACDC and BLND anomalies is that they are associated with shallow-seated (<3 km depth) dominantly SW-NE striking (50°NE) volcano-tectonic lineaments which focus fluid flow along shallow dipping (50° from the vertical) faults (Hudson et al., 2022).

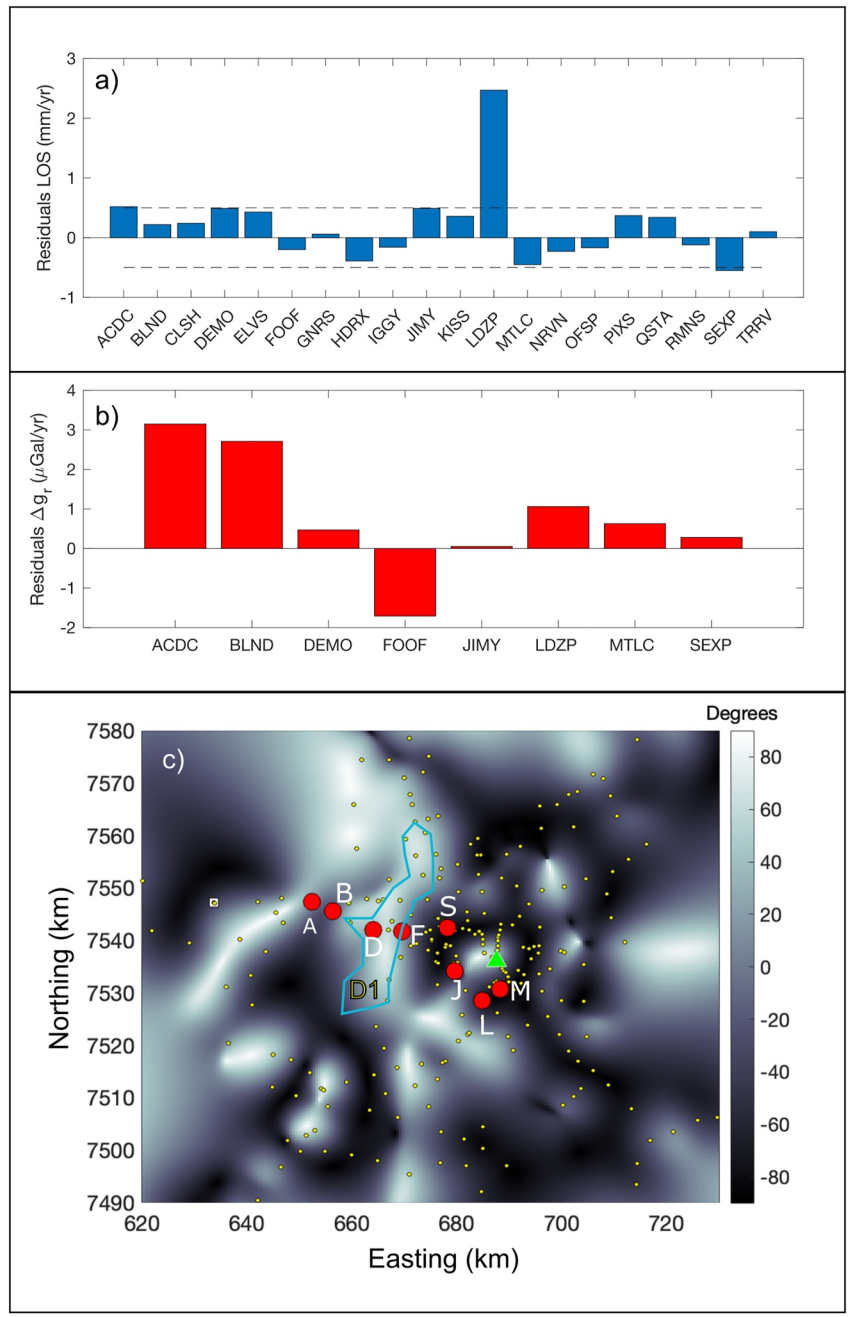

Figure 4. Model fits and interpretation. Mean annual residuals between model predictions and observations for 2014–2018 LOS displacements (mm/yr; Eiden et al., 2021) (a) and residual gravity changes (μGal/yr) 2010–2018 (b). Broken lines in (a) represent the typical uncertainty in the velocity data. The residual subsidence at LDZP is explained by a local deformation source in the Supporting Information. Uncertainties in the gravity data are ≥±5 μGal and not shown for clarity. (c) Gravimetric tilt angle derived from the local Bouguer anomaly using data presented in MacQueen et al. (2021) where angles are given in degrees. Small yellow circles mark static gravimetric measurement points. Red circles mark gravity benchmarks with longest temporal coverage (as shown in Figure 1). Labels A–M represent benchmark acronyms shown in (b). D1 indicates footprint of high-density anomaly modeled at 3 km a.s.l. (i.e., $z = -3$ km) by MacQueen et al. (2021). Benchmarks JIMY, LDZP, MTLC, and SEXP are located in a ring-like structure of high negative tilt angles and representative of the column-like low-density anomaly beneath Uturuncu (del Potro et al., 2013), whereas all other benchmarks, bar BLND, are located in structures with high positive tilt angles.

Although we have informed the models with available constraints on source dimensions and locations by other geophysical observations, which all rely on best-fit data modeling with inherent uncertainties, the results presented here only provide first-order insights into subsurface dynamics.

Smaller dimensions of the ABC ensemble than considered here would require larger density and pressure changes, with a larger ensemble requiring smaller changes. Given that we have used optimal model constraints we conclude that the results of the study fall in the range of geophysical solutions of a set of mutually consistent subsurface models of the target area (e.g., Comeau et al., 2016; del Potro et al., 2013; Hudson et al., 2022; Kukarina et al., 2017; MacQueen et al., 2021; McFarlin et al., 2017).

4. Conclusions

We propose a model of compressible transcrustal fluid transfer through a permeable upper crust (<25 km depth beneath the ground surface) as the source of anomalous ground deformation and gravity variations at Uturuncu volcano between 2010 and 2018. This model is consistent with only a minimal (undetectable) or no migration of magma from the APMB to shallower crustal levels during that time. Possible processes to explain the fluid release from the APMB include (a) a waning of magmatic activity in the APVC by the gradual crystallization of the APMB or (b) a trapping and subsequent release of ascending lower-crustal fluids in the APMB (Hudson et al., 2022). Both scenarios are inconsistent with the imminent renewal of volcanic activity at Uturuncu and more indicative of a waning of the magmatic activity in the APVC over the past 3 Ma (Salisbury et al., 2011).

In the absence of gravity change data prior to 2010 is difficult to assess whether the processes inferred in this study are also responsible for the substantially larger ground uplift of up to 10 mm yr^{-1} observed between 1965 and 2010 (Gottsmann et al., 2018; S. T. Henderson & Pritchard, 2013; Pritchard & Simons, 2004). This leaves the questions as to whether long-term unrest at Uturuncu be classed as magmatic, hydrothermal or hybrid unanswered. Our study, however, indicates a transcrustal contribution to unrest during the observation period and can perhaps be best described as hybrid in nature due to redistribution of magmatic fluids within a large and complex sub-volcanic plumbing system.

Our study demonstrates the benefit of pairing observations of spatiotemporal variations in the gravity field changes with measurements of surface deformation to provide insights into the evolution of restless volcanic systems. Recognizing transcrustal fluid migration as a source of volcanic unrest has important implications for the characterization of hydraulically connected sub-volcanic plumbing systems (Christopher et al., 2015; Journeau et al., 2022). It can also help explain the many non-eruptive episodes of volcano deformation world-wide (Biggs et al., 2014; Phillipson et al., 2013), and particularly those at large silicic calderas where similar linear trends between gravity changes and ground displacements have been noted (Williams-Jones & Rymer, 2002).

Data Availability Statement

The topographic data used in this study is from the Shuttle Radar Topography Mission (SRTM) 1 Arc-Second archive and is downloadable freely on https://earthexplorer.usgs.gov. The SRTM collections are located under the Digital Elevation category. The GNSS data from continuous station UTUR are available through UNAVCO at http://geodesy.unr.edu/NGLStationPages/stations/UTUR.sta. The gravity data are deposited at https://doi.org/10.5281/zenodo.6524352. The InSAR data are freely available to download from the Alaska Satellite Facility (https://asf.alaska.edu). To download, search Sentinel-1 data for the region and time period of interest. Sentinel-1 acquisition dates used in this study, along with processed InSAR data can be found at https://doi.org/10.5281/zenodo.6529578.

Acknowledgments
This work was funded by the Natural Environmental Research Council grants NE/G01843X/1 and NE/S008845/1, two NERC-Geophysical Equipment Facility instrument loans (910 and 928) and NSF grant EAR-1757495. M. Sunagua, R. del Potro, C. Muller, M. Diez, N. Young, R. Tintaya, G. Fernandez and F. Ticona facilitated and contributed to gravimetric data collection. SERGEOTECMIN, SERNAP, and the Observatorio San Calixto are thanked for providing field support. S. Henderson and P. MacQueen are thanked for providing guidance in InSAR processing. P. MacQueen also shared gradiometric data which helped with interpreting the findings of this study. The authors are grateful for constructive reviews by Craig Miller and an anonymous referee.

References

Afanasyev, A., Blundy, J., Melnik, O., & Sparks, S. (2018). Formation of magmatic brine lenses via focussed fluid flow beneath volcanoes. *Earth and Planetary Science Letters*, *486*, 119–128. https://doi.org/10.1016/j.epsl.2018.01.013

Agram, P. S., Jolivet, R., Riel, B., Lin, Y. N., Simons, M., Hetland, E., et al. (2013). New radar interferometric time series analysis toolbox released. *Eos Transactions American Geophysical Union*, *94*(7), 69–70. https://doi.org/10.1002/2013EO070001

Battaglia, M., Gottsmann, J., Carbone, D., & Fernandez, J. (2008). 4D volcano gravimetry. *Geophysics*, *73*(6), WA3–WA18. https://doi.org/10.1190/1.2977792

Berardino, P., Fornaro, G., Lanari, R., & Sansosti, E. (2002). A new algorithm for surface deformation monitoring based on small baseline differential SAR interferograms. *IEEE Transactions on Geoscience and Remote Sensing*, *40*(11), 2375–2383. https://doi.org/10.1109/TGRS.2002.803792

Bevis, M., Businger, S., Herring, T. A., Rocken, C., Anthes, R. A., & Ware, R. H. (1992). GPS meteorology: Remote sensing of atmospheric water vapor using the global positioning system. *Journal of Geophysical Research*, *97*(D14), 15787. https://doi.org/10.1029/92JD01517

Biggs, J., Ebmeier, S. K., Aspinall, W. P., Lu, Z., Pritchard, M. E., Sparks, R. S. J., & Mather, T. A. (2014). Global link between deformation and volcanic eruption quantified by satellite imagery. *Nature Communications*, *5*(1), 3471. https://doi.org/10.1038/ncomms4471

Brocher, T. M. (2005). Empirical relations between elastic wavespeeds and density in the Earth's crust. *Bulletin of the Seismological Society of America*, *95*(6), 2081–2092. https://doi.org/10.1785/0120050077

Cai, Y., & Wang, C.-Y. (2005). Fast finite-element calculation of gravity anomaly in complex geological regions. *Geophysical Journal International*, *162*(3), 696–708. https://doi.org/10.1111/j.1365-246x.2005.02711.x

Christopher, T. E., Blundy, J., Cashman, K., Cole, P., Edmonds, M., Smith, P. J., et al. (2015). Crustal-scale degassing due to magma system destabilization and magma-gas decoupling at Soufrière Hills volcano, Montserrat. *Geochemistry, Geophysics, Geosystems*, *16*(9), 2797–2811. https://doi.org/10.1002/2015GC005791

Comeau, M. J., Unsworth, M. J., & Cordell, D. (2016). New constraints on the magma distribution and composition beneath Volcán Uturuncu and the southern Bolivian Altiplano from magnetotelluric data. *Geosphere*, *12*(5), 1–31. https://doi.org/10.1130/GES01277.1

de Silva, S. L. (1989). Altiplano-Puna volcanic complex of the central Andes. *Geology*, *17*(12), 1102–1106. https://doi.org/10.1130/0091-7613(1989)017<1102:apvcot>2.3.co;2

Dehant, V., Defraigne, P., & Wahr, J. M. (1999). Tides for a convective Earth. *Journal of Geophysical Research: Solid Earth*, *104*(B1), 1035–1058. https://doi.org/10.1029/1998jb900051

del Potro, R., Díez, M., Blundy, J., Gottsmann, J., & Camacho, A. (2013). Diapiric ascent of silicic magma beneath the Bolivian Altiplano. *Geophysical Research Letters*, *40*(10), 2044–2048. https://doi.org/10.1002/grl.50493

Eiden, E., MacQueen, P., Henderson, S., & Pritchard, M. (2021). Multiple scales of deformation from geodetic monitoring point to active transcrustal magma system at Uturuncu volcano.

Farr, T. G., Rosen, P. A., Caro, E., Crippen, R., Duren, R., Hensley, S., et al. (2007). The Shuttle Radar Topography Mission. *Reviews of Geophysics*, *45*(2), RG2004. https://doi.org/10.1029/2005RG000183

Fialko, Y., & Pearse, J. (2012). Sombrero uplift above the Altiplano-Puna Magma Body: Evidence of a ballooning mid-crustal diapir. *Science*, *338*(6104), 250–252. https://doi.org/10.1126/science.1226358

Gottsmann, J., Blundy, J. D., Henderson, S., Pritchard, M. E., & Sparks, R. S. J. (2017). Thermomechanical modeling of the Altiplano-Puna deformation anomaly: Multiparameter insights into magma mush reorganization. *Geosphere*, *13*(4), 1042–1065. https://doi.org/10.1130/GES01420.1

Gottsmann, J., Muller, C., & del Potro, R. (2018). Fifty years of steady ground deformation in the Altiplano-Puna region of southern Bolivia. *Geosphere*, *14*(1), 65–73. https://doi.org/10.1130/GES01570.1

Henderson, S., & Setiawan, L. D. (2020). scottyhq/dinosar: Isce 2.3.3. *Zenodo*. https://doi.org/10.5281/zenodo.4033385

Henderson, S. T., & Pritchard, M. E. (2013). Decadal volcanic deformation in the central Andes volcanic zone revealed by InSAR time series. *Geochemistry, Geophysics, Geosystems*, *14*(5), 1358–1374. https://doi.org/10.1002/ggge.20074

Hickey, J., Gottsmann, J., & del Potro, R. (2013). The large-scale surface uplift in the Altiplano-Puna region of Bolivia; a parametric study of source characteristics and crustal rheology using Finite Element Analysis. *Geochemistry, Geophysics, Geosystems*, *15*(3), 540–555. https://doi.org/10.1002/ggge.20057

Hudson, T. S., Kendall, J. M., Pritchard, M. E., Blundy, J. D., & Gottsmann, J. H. (2022). From slab to surface: Earthquake evidence for fluid migration at Uturuncu volcano, Bolivia. *Earth and Planetary Science Letters*, *577*, 117268. https://doi.org/10.1016/j.epsl.2021.117268

Journeau, C., Shapiro Nikolai, M., Seydoux, L., Soubestre, J., Koulakov Ivan, Y., Jakovlev Andrei, V., et al. (2022). Seismic tremor reveals active trans-crustal magmatic system beneath Kamchatka volcanoes. *Science Advances*, *8*(5), eabj1571. https://doi.org/10.1126/sciadv.abj1571

Kukarina, E., West, M., Keyson, L. H., Koulakov, I., Tsibizov, L., & Smirnov, S. (2017). Focused magmatism beneath Uturuncu volcano, Bolivia: Insights from seismic tomography and deformation modeling. *Geosphere*, *13*(6), 1855–1866. https://doi.org/10.1130/GES01403.1

Lau, N., Tymofyeyeva, E., & Fialko, Y. (2018). Variations in the long-term uplift rate due to the Altiplano-Puna Magma Body observed with Sentinel-1 interferometry. *Earth and Planetary Science Letters*, *491*, 43–47. https://doi.org/10.1016/j.epsl.2018.03.026

Liang, C., Agram, P., Simons, M., & Fielding, E. J. (2019). Ionospheric correction of InSAR time series analysis of C-band Sentinel-1 TOPS data. *IEEE Transactions on Geoscience and Remote Sensing*, *57*(9), 6755–6773. https://doi.org/10.1109/TGRS.2019.2908494

Lucassen, F., Becchio, R., Harmon, R., Kasemann, S., Franz, G., Trumbull, R., et al. (2001). Composition and density model of the continental crust at an active continental margin—The central Andes between 21° and 27°S. *Tectonophysics*, *341*(1–4), 195–223. https://doi.org/10.1016/S0040-1951(01)00188-3

MacQueen, P., Gottsmann, J., Pritchard, M., Young, N., Ticona, J. E. T. T., & Tintaya, R. (2021). Dissecting a Zombie: Joint analysis of density and resistivity models reveals shallow structure and possible sulfide deposition at Uturuncu volcano, Bolivia. *Frontiers of Earth Science*, *9*, 725917. https://doi.org/10.3389/feart.2021.725917

McFarlin, H., Christensen, D., McNutt, S. R., Ward, K. M., Ryan, J., Zandt, G., & Thompson, G. (2017). Receiver function analyses of Uturuncu volcano, Bolivia and vicinity. *Geosphere*, *14*(1), 50–64. https://doi.org/10.1130/GES01560.1

Miller, H. G., & Singh, V. (1994). Potential field tilt—A new concept for location of potential field sources. *Journal of Applied Geophysics*, *32*(2), 213–217. https://doi.org/10.1016/0926-9851(94)90022-1

Morand, A., Brandeis, G., & Tait, S. (2021). Application of a plate model to reproduce surface deformations observed at Uturuncu volcano, Bolivia. *Journal of Volcanology and Geothermal Research*, *415*, 107241. https://doi.org/10.1016/j.jvolgeores.2021.107241

Phillipson, G., Sobradelo, R., & Gottsmann, J. (2013). Global volcanic unrest in the 21st century: An analysis of the first decade. *Journal of Volcanology and Geothermal Research*, *264*, 183–196. https://doi.org/10.1016/j.jvolgeores.2013.08.004

Pritchard, M. E., & Simons, M. (2004). An InSAR-based survey of volcanic deformation in the southern Andes. *Geophysical Research Letters*, *31*(L15610), L15610. https://doi.org/10.1029/2004GL020

Ray, R. (1999). A global ocean tide model from TOPEX/POSEIDON altimetry: GOT99. Technical Report NASA, 209478.

Rosen, P. A., Gurrola, E. M., Agram, P., Cohen, J., Lavalle, M., Riel, B. V., et al. (2018). The InSAR scientific computing environment 3.0: A flexible framework for NISAR operational and user-led science processing. In *IGARSS 2018—2018 IEEE International Geoscience and Remote Sensing Symposium* (pp. 4897–4900). https://doi.org/10.1109/IGARSS.2018.8517504

Salisbury, M. J., Jicha, B. R., de Silva, S. L., Singer, B. S., Jimenez, N. C., & Ort, M. H. (2011). Ar-40/Ar -39 chronostratigraphy of Altiplano-Puna volcanic complex ignimbrites reveals the development of a major magmatic province. *The Geological Society of America Bulletin*, *123*(5–6), 821–840. https://doi.org/10.1130/B30280.1

Sparks, R. S. J., Folkes, C. B., Humphreys, M. C. S., Barfod, D. N., Clavero, J., Sunagua, M. C., et al. (2008). Uturuncu volcano, Bolivia: Volcanic unrest due to mid-crustal magma intrusion. *American Journal of Science*, *308*(6), 727–769. https://doi.org/10.2475/06.2008.01

Van Camp, M., & Vauterin, P. (2005). Tsoft: Graphical and interactive software for the analysis of time series and earth tides. *Computers & Geosciences*, *31*(5), 631–640. https://doi.org/10.1016/j.cageo.2004.11.015

Ward, K. M., Zandt, G., Beck, S. L., Christensen, D. H., & McFarlin, H. (2014). Seismic imaging of the magmatic underpinnings beneath the Altiplano-Puna volcanic complex from the joint inversion of surface wave dispersion and receiver functions. *Earth and Planetary Science Letters*, *404*, 43–53. https://doi.org/10.1016/j.epsl.2014.07.022

Williams-Jones, G., & Rymer, H. (2002). Detecting volcanic eruption precursors: A new method using gravity and deformation measurements. *Journal of Volcanology and Geothermal Research*, *113*(3–4), 379–389. https://doi.org/10.1016/s0377-0273(01)00272-4

Yu, C., Li, Z., & Penna, N. T. (2018). Interferometric synthetic aperture radar atmospheric correction using a GPS-based iterative tropospheric decomposition model. *Remote Sensing of Environment*, *204*, 109–121. https://doi.org/10.1016/j.rse.2017.10.038

Yu, C., Li, Z., Penna, N. T., & Crippa, P. (2018). Generic atmospheric correction model for interferometric synthetic aperture radar observations. *Journal of Geophysical Research: Solid Earth*, *130*(10), 9202–9222. https://doi.org/10.1029/2017JB015305

Zandt, G., Leidig, M., Chmielowski, J., Baumont, D., & Yuan, X. (2003). Seismic detection and characterization of the Altiplano-Puna Magma Body, central Andes. *Pure and Applied Geophysics*, *160*(3–4), 789–807. https://doi.org/10.1007/pl00012557

References From the Supporting Information

Blewitt, G., Kreemer, C., Hammond, W. C., & Gazeaux, J. (2016). MIDAS robust trend estimator for accurate GPS station velocities without step detection. *Journal of Geophysical Research: Solid Earth*, *121*(3), 2054–2068. https://doi.org/10.1002/2015JB012552

Gudmundsson, A. (1983). Stress estimates from the length/width ratios of fractures. *Journal of Structural Geology*, *5*(6), 623–626. https://doi.org/10.1016/0191-8141(83)90075-5

Jay, J. A., Pritchard, M. E., West, M. E., Christensen, D., Haney, M., Minaya, E., et al. (2012). Shallow seismicity, triggered seismicity, and ambient noise tomography at the long-dormant Uturuncu volcano, Bolivia. *Bulletin of Volcanology*, *74*(4), 817–837. https://doi.org/10.1007/s00445-011-0568-7

Kösters, M. (1999). 3D-Dichtemodellierung des Kontinentalrandes sowie quantitative Untersuchungen zur Isostasie und Rigidität der Zentralen Anden (20°–26°S). In B. Reihe (Ed.), *Berliner geowissenschaftliche Abhandlungen* (Vol. 32).